colloids and interfaces

Article

The Shape Modulation of Laser-Induced Nanowelded Microstructures Using Two Colors

Ariel Rogers [1], Isabelle I. Niyonshuti [2], Jun Ou [3,4], Diksha Shrestha [1,5], Deborah Okyere [2,6], Jingyi Chen [2,6] and Yong Wang [1,5,6,*]

1 Department of Physics, University of Arkansas, Fayetteville, AR 72701, USA
2 Department of Chemistry and Biochemistry, University of Arkansas, Fayetteville, AR 72701, USA
3 School of Engineering, California State Polytechnic University Humboldt, Arcata, CA 95521, USA
4 Mechanical Engineering Program, California State Polytechnic University Humboldt, Arcata, CA 95521, USA
5 Cell and Molecular Graduate Program, University of Arkansas, Fayetteville, AR 72701, USA
6 Materials Science and Engineering Program, University of Arkansas, Fayetteville, AR 72701, USA
* Correspondence: yongwang@uark.edu

Abstract: The light-based nanowelding of metallic nanoparticles is of particular interest because it provides convenient and controlled means for the conversion of nanoparticles into microstructures and the fabrication of nanodevices. In this study, we investigated the wavelength dependence of laser-induced nanowelded shapes of silver nanoparticles (AgNPs). We observed that the nanowelded microstructures illuminated with only a 405 nm laser were more branched than those formed via illumination using both the 405 nm and 532 nm lasers. We quantified this observation by two compactness descriptors and examined the dependence of the power of the 532 nm laser. More importantly, to understand the experimental observations, we formulated and tested a hypothesis by calculating the wavelength-dependent electric field enhancement due to the surface plasmon resonance of the AgNPs and nanowelded microstructures when illuminated with lights at the two wavelengths. Based on the different patterns of hot spots for welding AgNPs from these calculations, numerical simulations successfully reproduced the different shapes of nanowelded microstructures, supporting our hypothesis. This work suggests the possibility of light-based control of the shapes of laser-induced nanowelded microstructures of metallic nanoparticles. This work is expected to facilitate the development of broader applications using the nanowelding of metallic nanoparticles.

Keywords: surface plasmon resonance; nanowelding; shape control; laser-induced assembly; metallic nanoparticles

Citation: Rogers, A.; Niyonshuti, I.I.; Ou, J.; Shrestha, D.; Okyere, D.; Chen, J.; Wang, Y. The Shape Modulation of Laser-Induced Nanowelded Microstructures Using Two Colors. *Colloids Interfaces* **2023**, *7*, 67. https://doi.org/10.3390/colloids7040067

Academic Editor: Reinhard Miller

Received: 13 September 2023
Revised: 1 November 2023
Accepted: 6 November 2023
Published: 9 November 2023

1. Introduction

Due to the broad applications of metallic nanoparticles in photonics, electronics, and the fabrication of nanodevices [1–9], welding between nanoparticles (termed nanowelding) has been of great interest [10–19]. For example, nanowelding is an attractive strategy to significantly reduce the contact resistance between nanoparticles due to the capping layer of the nanoparticles during synthesis, creating solid nanocontact for efficient electron transport and facilitating the fabrication of effective nanodevices [10–14]. The nanowelding of nanomaterials has been achieved through various methods, including thermal heating, pressure, laser/light, electric current/field, and plasma [15,20–23]. Among these methods, the laser/light-based nanowelding has been particularly interesting to many researchers due to its noncontact and noninvasive nature, the convenience and ease of use, the wide range of choices of light wavelength, and the capability of nanowelding at room temperature [10–12,16,24–28]. For instance, shining lasers or fluorescent lights on metallic nanoparticles could weld them into higher-order assemblies and microstructures or change their shapes in a controlled manner [11,24–27].

Light-based nanowelding relies on localized surface plasmon resonance (SPR) in metallic nanoparticles [10,12,24–26]. SPR refers to the coherent oscillations of free electrons on the surface of metals, coupled to the electromagnetic waves of the incident light [29–32]. Because SPR is dependent on the size, shape, and composition of nanoparticles, lights with appropriate wavelengths (i.e., around the resonance wavelength) are required to generate localized SPR for nanowelding for a given type of metallic nanoparticles [24,25,33,34]. Therefore, a single wavelength of light (or a narrow bandwidth) was typically used for light-based nanowelding in the past, while the wavelength dependence of the nanowelding of metallic nanoparticles has been rarely studied [10,15,28,33,35,36].

We set out to investigate how the shapes of nanowelded microstructures of metallic nanoparticles depend on the light wavelength. The rationale of this work is two-fold. First, an advantage of light-based nanowelding lies in the wide range of wavelengths of light [33], while understanding the wavelength dependence of laser-induced nanowelded shapes of metallic nanoparticles is expected to allow us to exploit this advantage. Second, although single metallic nanoparticles (of given shape, size, and composition) have distinct resonance wavelengths, nanowelded assemblies and microstructures have different shapes and sizes, and thus they will likely show different SPR responses to different wavelengths [24,25,33].

In this study, we used silver nanoparticles (AgNPs) as a model and investigated the wavelength dependence of laser-induced nanowelded microstructures of AgNPs. AgNPs were used in our previous study for examining the real-time kinetics of laser-induced nanowelding, in which we observed that AgNPs illuminated with a 405 nm laser formed branched microstructures [12]. Here, we illuminated the AgNPs with an additional laser at 532 nm and observed the shapes of nanowelded microstructures using fluorescence microscopy. We also varied the power of the 532 nm laser and quantified how the shape of nanowelded microstructures depended on the power. More importantly, to understand the experimental observations, we formulated and tested a hypothesis by examining the wavelength-dependent electric field enhancement due to the SPR of both individual AgNPs and nanowelded microstructures when illuminated with lights at the two wavelengths.

2. Materials and Methods

2.1. Synthesis and Characterization of AgNPs

The AgNPs used in this study were synthesized using the polyol method [37], following the same procedures as in our previous studies [12,38–40]. Briefly, 50 mL of ethylene glycol (EG, J.T. Baker/Avantor, Radnor, PA, USA) was added to a 250 mL 3-neck round bottom flask and heated to 150 °C in an oil bath, followed by adding 0.6 mL of 3 mM NaHS (Alfa Aesar, Ward Hill, MA, USA) in EG, 5 mL of 3 mM HCl (Alfa Aesar, Ward Hill, MA, USA) in EG, 12 mL of 0.25 g polyvinylpyrrolidone (PVP, MW ~55,000, Sigma-Aldrich, Burlington, VT, USA) in EG, and 4 mL of 282 mM CH_3COOAg (Alfa Aesar, Ward Hill, MA, USA). The reaction proceeded at 150 °C for ~1 h until the absorbance peak position (measured via UV–Vis spectroscopy) reached ~420 nm. The reaction was then quenched by placing the flask in an ice bath. Acetone was added to the mixture at a 5:1 volume ratio, and the product was collected via centrifugation. The resultant AgNPs were purified using water, collected via centrifugation, and resuspended in water for characterization and future use, while the concentration was determined using inductively coupled plasma mass spectrometry (ICP-MS; iCAP RQplus mass spectrometer, Thermo Fisher Scientific, Waltham, MA, USA).

The synthesized AgNPs were characterized via transmission electron microscopy (TEM) and UV–Vis spectrometry. TEM images were captured using a TEM microscope (JEOL JEM-1011, JEOL USA, Peabody, MA, USA) with an accelerating voltage of 100 kV. Particle size and shape were measured on the TEM images using ImageJ (Version: 2.3.0/1.53q) and an algorithmic analysis reported by Laramy et al. [41]. UV–Vis spectra were obtained using a UV–Vis spectrophotometer (Cary 50, Agilent Technologies, Santa Clara, CA, USA).

2.2. Fluorescence Microscopy for Imaging of Nanowelded Microstructures of AgNPs

The prepared AgNPs were first diluted in ultrapure water (≥17.5 MΩ·cm) to a final concentration of 1.3 mg/mL and then added to a flow chamber made of cleaned coverslips and glass slides [12,39,40,42,43]. The flow chamber was sealed using nail polish and then mounted on a fluorescence microscope for imaging (Figure 1A) [42]. Note that the conjugation of fluorescent dyes to the surface of the AgNPs was not needed as AgNPs are fluorescent by themselves [12,44,45]. The fluorescence microscope used in this study was an Olympus (Center Vally, PA, USA) IX-73 inverted microscope equipped with an Olympus 100 × NA = 1.49 oil immersion TIRF objective, a multi-color laser bank (iChrome MLE, Toptica Photonics, Pittsford, NY, USA), and an EMCCD camera (iXon Ultra 897, Andor Technology, Belfast, UK), similar to our previous study [12]. A 405 nm laser and a 532 nm laser from the laser bank were used in this study. The microscope and data acquisition were controlled using Micro-Manager [46,47]. A BrightLine full-multiband 1λ P-V RWE super-resolution laser filter set (LF405/488/532/635-B-000, Semrock, Lake Forest, IL, USA) was used in the emission path of the microscope. The laser-induced nanowelded microstructures of AgNPs were imaged on the EMCCD camera. The effective pixel size of acquired images was 160 nm. To facilitate comparisons among measurements under different conditions, videos of 6000 frames were taken. The lasers were turned on at time 0 (i.e., frame 0 of the recorded videos), while the last frame of each movie was used for further analysis. The total exposure time to lasers was 5.25 min.

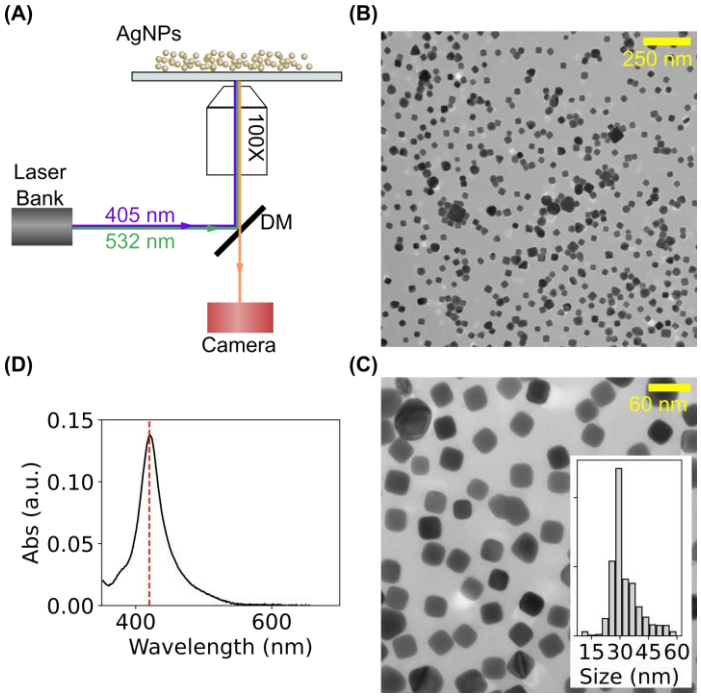

Figure 1. Experimental setup and characterization of AgNPs: (**A**) sketch of the experimental setup for visualizing nanowelded microstructures using fluorescence microscopy; (**B**,**C**) representative TEM images of AgNPs used in this study. The inset of panel C shows the size distribution of the AgNPs used in this study; (**D**) absorption spectrum measured using a UV–Vis spectrometer. The red dashed line indicates 420 nm.

2.3. TEM Imaging of Nanowelded Microstructures

AgNPs in ultrapure water at a concentration of 1.3 mg/mL were added to a TEM grid placed in a Petri dish with a coverslip bottom. The sample was mounted on the fluorescence microscope and illuminated with the 405 nm laser for 5.25 min. The TEM grid with formed assemblies of AgNPs was then imaged using a TEM microscope (JEOL JEM-1011, JOEL USA, Peabody, MA, USA) with an accelerating voltage of 100 kV.

2.4. Automatic Identification of Nanowelded Microstructures of AgNPs

The laser-induced nanowelded microstructures were identified automatically using custom Python scripts based on the scikit-image Python package [48], as described in our previous work [12]. For the last frame of the videos, the background was first removed using a rolling-ball algorithm [49] with a ball size of 9 pixels, followed by smoothing twice using a Gaussian filter with a standard deviation of 1 pixel. The background in the smoothed image was removed once again, followed by applying a threshold to obtain a black/white (BW) image. Edges were detected from the BW image using the Sobel filter [50], followed by dilating the edges by 3 pixels to fill possible gaps in the edges. Small objects with areas <32 pixels were removed, before performing a flood fill [51]. The filled objects were eroded with 4 pixels, followed by removing small objects (area <32 pixels). The resulting BW image was segmented into individual structures, which corresponded to the identified microstructures. The boundaries of the microstructures were recorded as $n \times 2$ arrays, $B = \begin{pmatrix} x_1, & x_2, & \cdots, & x_n \\ y_1, & y_2, & \cdots, & y_n \end{pmatrix}^T$.

2.5. Shape Analysis of the Nanowelded Microstructures of AgNPs

The shapes of the nanowelded microstructures of AgNPs were analyzed and compared based on two compactness descriptors [52]. The first compactness descriptor is the coverage coefficient Ω, defined as the covering percentage of the microstructure over its circumscribed circle. In more detail, for a given microstructure described by its boundary B, the area of the microstructure A was calculated using the Gauss's area formula [53]. The radius of the circumscribed circle of the microstructure was determined as $r_m = \max\left(\sqrt{(x_i - x_c)^2 + (y_i - y_c)^2}\right)$, where $x_c = \sum_{i=1}^{N} \frac{x_i}{n}$ and $y_c = \sum_{i=1}^{N} \frac{y_i}{n}$ are the position of the center of mass of the microstructure. Then, the coverage coefficient was estimated as $\Omega = \frac{A}{\pi r_m^2}$. The second compactness descriptor is the roughness coefficient σ [52,54]. For a given microstructure with boundary B, we calculated the distance of vertices to the center of mass, $r = \sqrt{(x_i - x_c)^2 + (y_i - y_c)^2}$, and estimated the standard deviation, σ_r. To facilitate the comparison among microstructures of different sizes, the roughness coefficient was normalized using the perimeter (P), $\sigma = \sigma_r / P$, where $P = \sum_{i=1}^{n} \sqrt{(x_i - x_{i-1})^2 + (y_i - y_{i-1})^2}$.

2.6. Calculation of Electric Field Enhancement

The electric field enhancement on the surfaces of a single AgNP and a cross-shaped microstructure (AgCS) in water was calculated using the MNPBEM17 toolbox [55–57]. The refractive index of bulk silver from the toolbox was used, while the refractive index of water was taken to be 1.33. Electromagnetic plane waves of linear polarization were used for excitation, and the electric field enhancement was computed by summing the incoming and induced electric fields [55–57]. The polarization was either in x or y direction, while the wavelength was either 405 nm or 532 nm. For each wavelength, the total electric fields were calculated by averaging the electric field enhancement in both polarization directions. When the AgNP or AgCS was illuminated with both lasers, the electric field enhancement from both wavelengths were added up.

2.7. Simulation of Growth of Microstructures

Numerical simulations were run to examine the shapes of the microstructures when different locations of the microstructures (faces vs. multifaceted grooves) showed different probabilities of welding additional AgNPs. Briefly, an empty square grid (30×30) was prepared with a single AgNP placed at the center as the seed. Then, 20 additional AgNPs were welded sequentially one by one, following three rules: (1) Each new AgNP can only be placed next to the microstructure (i.e., the new location for welding must have a neighboring occupied site); (2) the probability of welding the new AgNP to a multifaceted-groove location (i.e., with multiple neighboring occupied sites) is P_m, and the probability of placing it on a microstructure face (i.e., with a single neighboring occupied site) is $1 - P_m$;

(3) if multiple candidate sites are possible, a random candidate site is chosen for welding the new AgNP. For each value of P_m, 1000 simulations were run, generating 1000 different shapes. The shapes were analyzed as described above. We also varied P_m from 0.05 to 0.95 and compared the compactness descriptors (e.g., coverage Ω) for different P_m values.

3. Results and Discussion

The AgNPs used in this study were characterized as described previously and shared the same characteristics as those in our previous study [12]. TEM images showed that the AgNPs were mostly nanocubes, while a small fraction (~23%) appeared as nanospheres and nanotriangles (Figure 1B,C). The average size of the AgNPs was measured to be 32 ± 8 nm (measured from 674 AgNPs, inset of Figure 1C), consistent with our previous study [12]. The absorption spectrum of the AgNPs was measured via UV–Vis spectroscopy, showing a peak at 420 nm [12] (Figure 1D).

As reported previously, microscale higher-order structures and assemblies of AgNPs were formed upon illumination with a 405 nm laser due to SPR [12]. The wavelength of 405 nm was chosen as it is close to the SPR peak of the AgNPs [12] (Figures 1D and S1). These microstructures could be visualized using fluorescence microscopy (Figure 2A), as the fluorescence intensities of the higher-order microstructures were stronger than those of the individual AgNPs [12]. With the 405 nm laser illumination, the formed microstructures showed branches (Figure 2A–D), which could be explained with a simple analytical model based on polymerization [12]. Such branched microstructures were confirmed using TEM, as shown in Figure 2E–H [12]. High-resolution TEM measurements were also performed on these microstructures, showing that the AgNPs were indeed fused/nanowelded into each other and displayed lattice fringes across the interfaces [12]. It should be noted that, although TEM results showed much higher resolution and more details of the nanowelded microstructures of AgNPs, the field of view was compromised compared with fluorescence microscopy (Figure 2). A single microstructure may exceed the TEM field of view (Figure 2E). For convenience, fluorescence microscopy was chosen in this study to further investigate the wavelength dependence of laser-induced nanowelding of AgNPs.

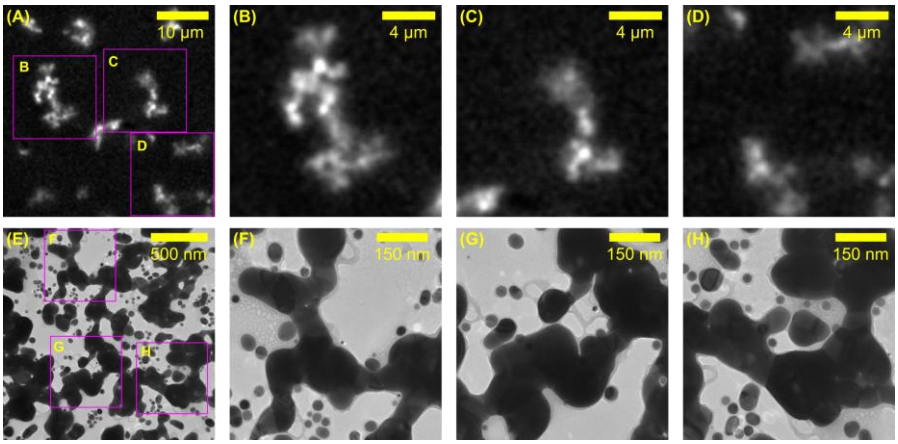

Figure 2. Laser-induced nanowelding of AgNPs with 405 nm laser illumination: (**A**) representative fluorescence image of laser-induced assemblies of AgNPs when illuminated with a 405 nm laser; (**B**–**D**) zoomed-in images of the corresponding regions in panel A; (**E**) representative TEM image of the laser-induced assemblies of AgNPs when illuminated with a 405 nm laser; (**F**–**H**) zoomed-in images of the corresponding regions in panel (**E**).

We then visualized the nanowelded microstructures formed by the AgNPs after being illuminated with a 405 nm laser, in the absence or presence of a 532 nm laser at different powers. The 532 nm laser was chosen because we expected that the nanowelded microstructures respond to longer wavelengths as larger AgNPs showed redshifts in their

scattering/absorption spectra [58–60] (Figure S1). Representative images of the nanowelded microstructures are shown in Figure 3. Compared with the branched microstructures with 405 nm laser illumination only (Figures 2 and 3A,G) [12], the nanowelded microstructures became more compact and less branched when the AgNPs were illuminated with both the 405 nm and 532 nm lasers (Figure 3B–F,H–L). Note that little nanowelding was observed with the 532 nm laser alone. We should also point out that varying the power of the 405 nm laser alone changed the nanowelding kinetics but resulted in similar branched microstructures [12].

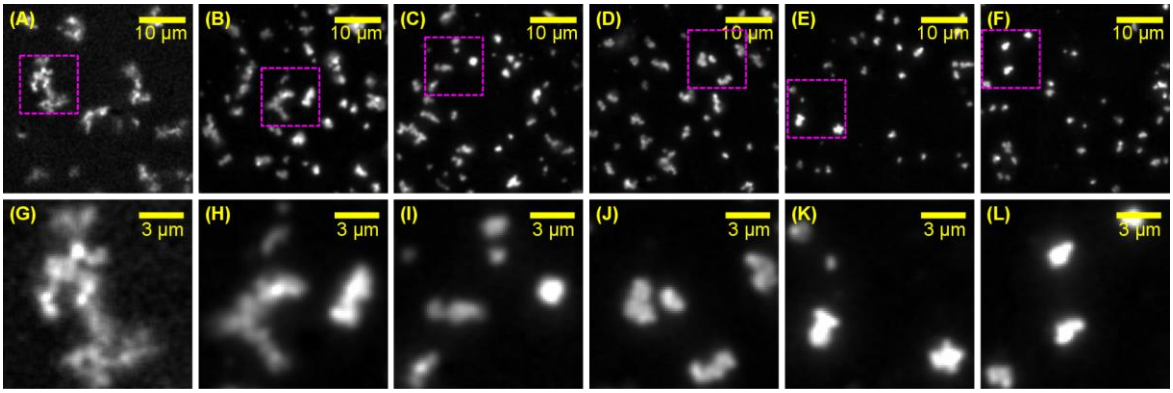

Figure 3. Representative images of nanowelded microstructures of AgNPs when illuminated with 405 nm laser of fixed power at ~3.60 mW in combination with 532 nm laser of different powers: (**A**,**G**) 0% (0 mW), (**B**,**H**) 20% (~6.00 mW), (**C**,**I**) 40% (~12.85 mW), (**D**,**J**) 60% (~20.00 mW), (**E**,**K**) 80% (~28.2 mW), and (**F**,**L**) 100% (~36.3 mW). Images in the bottom row (**G**–**L**) are zoomed-in images of the magenta, square regions of the top-row images (**A**–**F**).

To quantify this observation, we identified the nanowelded microstructures from the images and examined the compactness of the microstructures based on two compactness descriptors [52]. The first descriptor is the coverage coefficient Ω, defined as the covering percentage of the microstructure over its circumscribed circle (Figure 4A). A branched structure is expected to have a lower coverage coefficient than a more compact structure. As shown in Figure 4A, the coverage coefficient of nanowelded microstructures steadily increased from 49% to 65% as the power of the 532 nm laser increased from 0% to 100%. The second compactness descriptor is the roughness coefficient, σ, defined as the standard deviation of the distance of boundary points to the center of the microstructure normalized by the perimeter of the microstructure [52,54]. As branches on a microstructure will result in rougher peripheries, larger fluctuations, and thus larger standard deviations, we expect that a microstructure with more branches has a higher roughness coefficient than more compact ones [52]. As expected, the roughness coefficient decreased from 0.031 to 0.019 as the power of the 532 nm laser increased from 0% to 100% (Figure 4B).

To understand the observed different nanowelded shapes of AgNPs without and with the 532 nm laser (in addition to the 405 nm laser), we hypothesized that, when illuminated with lights of different wavelengths, the surface plasmon resonance of the AgNPs and nanowelded microstructures produced different patterns of hot spots for the nanowelding of additional AgNPs. To test this hypothesis, we calculated the enhancement of the electric field at the surfaces of a single AgNP and a cross-shaped microstructure (AgCS), using a boundary element method (BEM) approach with the MNPBEM17 toolbox [55–57]. The AgNP was modeled as a 30 × 30 × 30 nm nanocube (Figure 5A), while the AgCS consisted of five nanocubes, with a dimension of 90 × 90 × 30 nm (Figure 5B). The scattering spectra of the AgNP and the AgCS were determined using the MNPBEM17 toolbox [55–57], showing a peak of 431 nm for the AgNP (Figure 5C, black solid line), consistent with our previous result based on the discrete dipole approximation (DDA) method using the DDSCAT 7.3 program [12,61,62]. For the AgCS, we observed a primary peak at 645 nm, with a

secondary peak at 419 nm (Figure 5C, red dotted line). It is well known that a larger size of nanoparticles results in a redshift [58–60]. Therefore, due to the larger overall size of the AgCS compared with the individual AgNPs, the redshift of the primary peak is expected. The emergence of the secondary peak is likely due to the special shape of the AgCS.

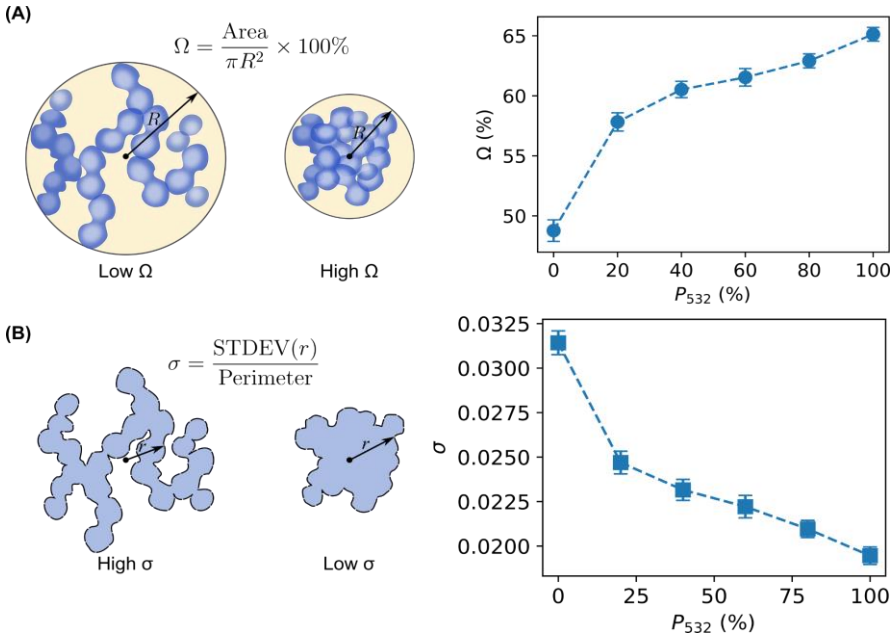

Figure 4. Compactness analysis of the nanowelded microstructures of AgNPs: (**A**) dependence of the coverage Ω of the nanowelded microstructures on the power of the 532 nm laser; (**B**) dependence of the roughness coefficient σ of the nanowelded microstructures on the power of the 532 nm laser. Error bars in both panels stand for the standard errors of the means (SEM). The number of measurements per sample ranged from 245 to 435.

We further calculated the electric field enhancement at the surfaces of the AgNP and the AgCS when illuminated with the 405 nm laser and/or the 532 nm laser using the MNPBEM17 toolbox [55–57]. Linearly polarized plane waves (in x or y direction) with wavelengths of 405 nm or 532 nm were used. Near-field electronic polarization has been a major topic for studying SPR [63–65]. The electric field enhancement (averaged over the two polarization directions) of the AgNP and the AgCS at the Z = 0 nm planes are shown in Figure 5D,E, respectively. For the outside of the individual AgNPs, we observed that the electric field enhancement was more significant at the faces of the AgNPs with the 405 nm laser illumination, while it was more significant at the edges/corners with the 532 nm laser illumination (Figure 5D). The difference is more significant when comparing the inside of the AgNPs: The electric field "penetrated" into, and was enhanced inside, the AgNP when excited with the 405 nm laser alone—an indication of the resonance—while illumination with the 532 nm laser alone did not show any electric field enhancement (Figure 5D). This difference is consistent with the measured and calculated spectra of the individual AgNPs (Figures 1D and 5C). With both lasers of equal amplitude, the total electric field enhancement around the AgNP was roughly uniform (Figure 5D). The difference in the distribution of electric field enhancement with different illuminations was also obvious for the AgCS (Figure 5E). With the 405 nm laser illumination, the electric field enhancement was significant at the faces of the AgCS. In contrast, the grooves (concave corners) of the AgCS showed the highest electric field enhancement with the 532 nm laser illumination (Figure 5E). In addition, with both lasers of each amplitude, the multifaceted grooves of the AgCS continued to show the highest electric field enhancement (Figure 5E). Additionally, it was observed that the electric field was enhanced inside the AgCS for both illuminations

at 405 nm alone and 532 nm alone, consistent with the calculated spectrum of the AgCS (Figure 5C).

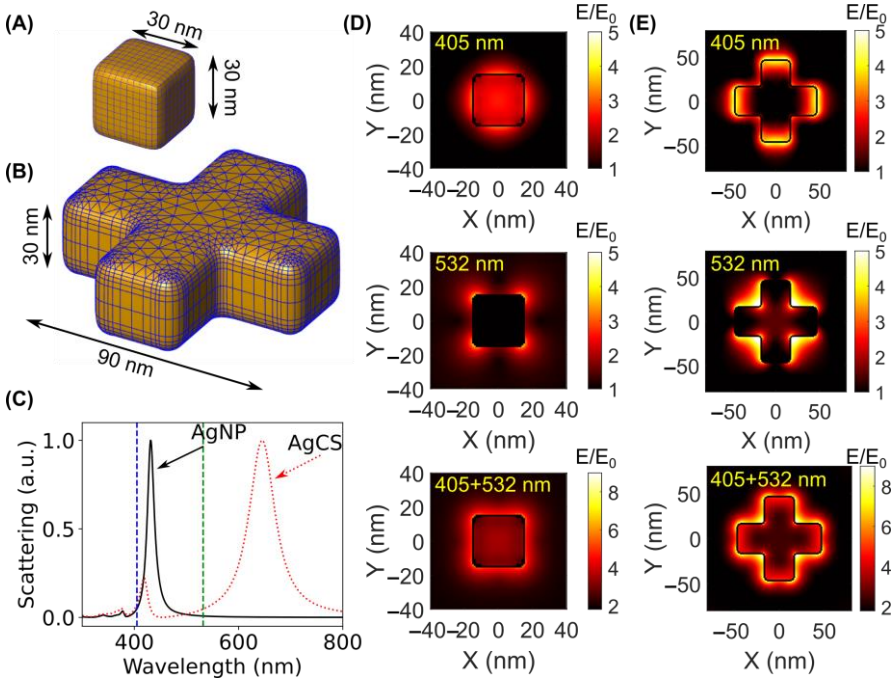

Figure 5. Electric field enhancement due to surface plasmon resonance at the surfaces of a single AgNP and a nanowelded cross-shaped microstructure: (**A**,**B**) the geometry of (**A**) a single AgNP and (**B**) a nanowelded cross-shaped microstructure (AgCS). Blue lines indicate the edges of the boundary elements generated with the MNPBEM17 toolbox [55–57]; (**C**) the calculated scattering spectra (rescaled) of the single AgNP and the cross-shaped AgCS; the blue and green lines indicate 405 nm and 532 nm, respectively; (**D**) the calculated electric field enhancement of the single AgNP when illuminated with (**top**) 405 nm laser only, (**middle**) 532 nm laser only, and (**bottom**) 405 and 532 nm lasers; (**E**) the calculated electric field enhancement of the cross-shaped AgCS when illuminated with (**top**) 405 nm laser only, (**middle**) 532 nm laser only, and (**bottom**) 405 and 532 nm lasers.

To further test our hypothesis, we developed a model and numerically simulated the nanowelding growth of microstructures based on the different patterns of electric field enhancement with different illuminations. Because the generated heat is proportional to the square of the electric field ($Q \sim \sigma_{Ag} E^2$, where σ_{Ag} is the conductivity of silver, and E is the electric field) [2], different patterns of electric field enhancement would result in different patterns of temperature enhancement (i.e., "hot spots") at the surfaces of the AgNPs and nanowelded microstructures. Thus, the hot spots would lead to different melting patterns and probabilities for welding new/additional AgNPs. Based on the calculations above, we, therefore, modeled that illumination with a single laser at 405 nm led to a higher probability of attaching new AgNPs to the faces of the microstructures (and a lower probability to grow at the multifaceted grooves—low P_m), while illumination with both lasers (405 nm and 532 nm) resulted in a higher probability of welding new AgNPs to the multifaceted grooves of the microstructures (high P_m, Figure 6A). A total of 1000 simulations were run for each case (i.e., 405 nm only vs. 405 nm + 532 nm), while the final size of microstructures was set to 21. Representative images of the simulated microstructures are shown in Figure 6B, where the top row shows the results for $P_m = 0.1$ (i.e., illumination with 405 nm only), and the bottom row shows the results for $P_m = 0.9$ (i.e., illumination with 405 nm + 532 nm). More representative simulated images with different P_m values are shown in Figure S2. We observed that illumination with a single laser at 405 nm resulted in branched structures (top row of Figure 6B), while illumination with both lasers led to compact structures (bottom row of Figure 6B), consistent with

our experimental results (Figure 3). Furthermore, we quantified the compactness of the simulated microstructures in each case using the coverage coefficient Ω and observed that the coverage coefficient increased as the P_m increased (Figure 6C), again consistent with the experimental results (Figure 4).

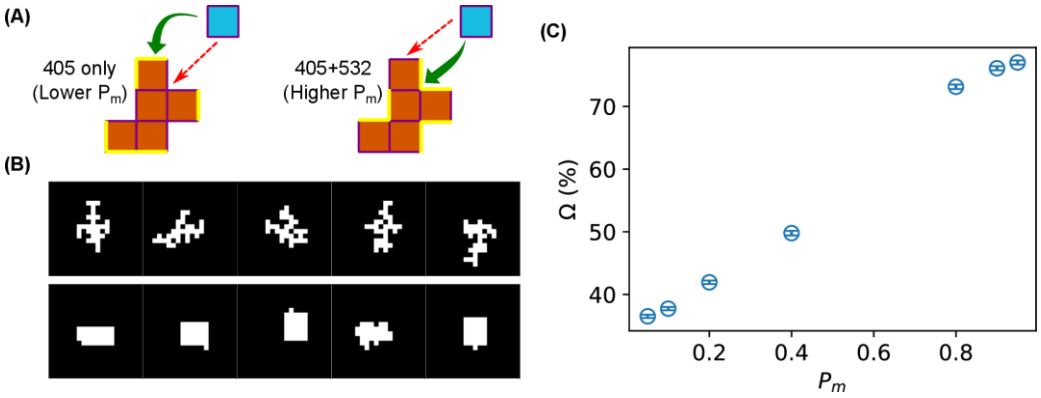

Figure 6. Simulation of different shapes of nanowelded microstructures based on the differences in the SPR-induced electric field enhancement: (**A**) model for the growth of nanowelded microstructures with different probabilities of growing at the corners (i.e., newly attached AgNP is adjacent to multiple faces), P_m. The yellow edges highlight the preferences of attachment of new AgNPs with low (**left**) or high (**right**); (**B**) representative shapes of nanowelded microstructures with (**top**) $P_m = 0.1$ and (**bottom**) $P_m = 0.9$; (**C**) dependence of the coverage Ω of the simulated nanowelded microstructures on P_m.

4. Conclusions

In conclusion, we investigated the wavelength dependence of laser-induced nanowelded shapes of AgNPs. We observed that the nanowelded microstructures of AgNPs illuminated with the 405 nm laser only were more branched than those formed via illumination with both the 405 nm and 532 nm lasers (Figure 3). We quantified this observation using two compactness descriptors and examined the dependence of the power of the additional 532 nm laser (Figure 4). More importantly, to understand the experimental observations, we formulated and tested a hypothesis that the surface plasmon resonance of the AgNPs and nanowelded microstructures generated different patterns of hot spots for the nanowelding of additional AgNPs when illuminated with lights of different wavelengths. This hypothesis was supported by the calculations of the wavelength-dependent electric field enhancement due to surface plasmon resonance of the AgNPs and nanowelded microstructures when illuminated with lights at the two wavelengths (Figure 5). Based on the different patterns of hot spots for welding additional AgNPs from these calculations, we ran numerical simulations and successfully reproduced different shapes of nanowelded microstructures (Figure 6), supporting our hypothesis.

It is worth noting that, in addition to nanowelded AgNPs showing different surface plasmonic properties from individual AgNPs (Figure 5), it is well known that adjacent AgNPs without welding could change the electric field enhancement [29,66]. For example, as shown in Figure S3, calculations using the MNPBEM17 package revealed that not only the spectra of the two AgNPs were different from the single AgNP in a separation-dependent manner but also hot spots were formed between the two AgNPs. Such effects likely play a role in the observed wavelength-dependent nanowelding of AgNPs. It would be exciting to see a more complete model developed in the future.

Fluorescence imaging has been used in our studies to examine the nanowelded microstructures of AgNPs [12], which was possible due to the photoluminescence of AgNPs [39,45,67]. TEM imaging was used to confirm the nanowelding of AgNPs in our previous work and this study [12]. Although the resolution of TEM is much higher than fluorescence imaging, the latter provides a much larger field of view. Therefore, compared

with electron microscopy, fluorescence microscopy is simple, versatile, and convenient. As other metallic nanoparticles (e.g., gold and copper nanoparticles) are also photoluminescent [68–73], we expect that the methods exploited in the current study are readily applicable to the studies of nanowelding of other metallic nanoparticles. On the other hand, we should point out that AgNPs were chosen in the current study because silver can support strong surface plasmon across a wider spectrum, from 300 nm to 1200 nm, than other metals, including gold and copper [29,32]. For nanoparticles composed of other metals, the wavelengths used for nanowelding would be different. For example, the resonance wavelength of individual gold nanoparticles of 30 nm is around 560 nm, while the wavelength for cross-shaped structures is around 720 nm (Figure S4).

It is well known that the scattering spectra and surface plasmon resonance of metal nanoparticles strongly depend on their material, composition, size, and shape, as well as the surrounding dielectric environment [74,75]. It would be exciting to examine the laser-induced nanowelding of nanoparticles comprising different metals, and with different sizes and shapes. It would also be interesting to investigate how different solutions affect the nanowelding process. We expect that the MNPBEM17 toolbox [55–57] will be useful for the rational design of different nanowelding patterns based on laser and metal nanoparticles by tuning the properties of dielectric solutions; the material, size, and shape of nanoparticles; and the wavelength of illumination. In the current work, the simulations and calculations of the electric field enhancement were performed on individual AgNPs and cross-shaped structures, in combination with growth simulations, as a starting point to understand the wavelength dependence of AgNP nanowelding. However, it would be interesting to simulate the surface plasmonic properties of microscale structures of AgNPs in different configurations and organizations in the future.

The current work suggests that it is possible to control the shapes of laser-induced nanowelded microstructures of metallic nanoparticles using light at different wavelengths. This capability of the light-based control of nanowelded shapes is expected to be convenient for various applications, such as conductive bonding [15,76,77] and nanoparticle-based metal printing [78–80]. Our study is expected to provide a better understanding and control of such applications. We found that the observed wavelength-dependent nanowelded shapes were associated with the wavelength dependence of the electric field enhancement or the surface plasmon resonance. It would be interesting to theoretically and experimentally explore the dependence of nanowelded shapes of metallic nanoparticles on a wider range of wavelengths. We expect that such work will facilitate the rational design of different shapes using illumination at different wavelengths.

Supplementary Materials: The following supporting information can be downloaded at: https://www.mdpi.com/article/10.3390/colloids7040067/s1.

Author Contributions: Conceptualization, Y.W.; methodology, A.R., I.I.N., J.O., D.S., J.C. and Y.W.; software, A.R., J.O. and Y.W.; validation, A.R., I.I.N., D.S. and D.O.; formal analysis, A.R., I.I.N., J.O., D.S., D.O. and Y.W.; investigation, A.R., I.I.N., D.S. and D.O.; resources, J.C. and Y.W.; data curation, A.R., I.I.N., J.O., J.C. and Y.W.; writing—original draft preparation, A.R. and Y.W.; writing—review and editing, A.R., I.I.N., J.O., D.S., D.O., J.C. and Y.W.; visualization, A.R., I.I.N., J.O. and Y.W.; supervision, J.C. and Y.W.; project administration, Y.W.; funding acquisition, J.C. and Y.W. All authors have read and agreed to the published version of the manuscript.

Funding: This research was partially supported by the National Science Foundation, grant number 1826642; the National Institute of Food and Agriculture/United States Department of Agriculture, grant number 2021-67019-33683; and the Arkansas Biosciences Institute.

Data Availability Statement: The data presented in this study are available on request from the corresponding author.

Acknowledgments: We acknowledge the support from the Arkansas High Performance Computing Center, which was supported by multiple National Science Foundation grants and the Arkansas Economic Development Commission.

Conflicts of Interest: The authors declare no conflict of interest.

References

1. Ferrera, M.; Della Valle, G.; Sygletou, M.; Magnozzi, M.; Catone, D.; O'Keeffe, P.; Paladini, A.; Toschi, F.; Mattera, L.; Canepa, M.; et al. Thermometric Calibration of the Ultrafast Relaxation Dynamics in Plasmonic Au Nanoparticles. *ACS Photonics* **2020**, *7*, 959–966. [CrossRef]
2. Govorov, A.O.; Richardson, H.H. Generating Heat with Metal Nanoparticles. *Nano Today* **2007**, *2*, 30–38. [CrossRef]
3. Li, H.; He, Y.; Wang, C.; Wang, X.; Hu, Y. Tunable Thermal and Electricity Generation Enabled by Spectrally Selective Absorption Nanoparticles for Photovoltaic/Thermal Applications. *Appl. Energy* **2019**, *236*, 117–126. [CrossRef]
4. Naito, M.; Yokoyama, T.; Hosokawa, K.; Nogi, K. *Nanoparticle Technology Handbook*; Elsevier: Amsterdam, The Netherlands, 2018; ISBN 978-0-444-64111-3.
5. Praetorius, A.; Scheringer, M.; Hungerbühler, K. Development of Environmental Fate Models for Engineered Nanoparticles—A Case Study of TiO_2 Nanoparticles in the Rhine River. *Environ. Sci. Technol.* **2012**, *46*, 6705–6713. [CrossRef]
6. Sarina, S.; Waclawik, E.R.; Zhu, H. Photocatalysis on Supported Gold and Silver Nanoparticles under Ultraviolet and Visible Light Irradiation. *Green Chem.* **2013**, *15*, 1814–1833. [CrossRef]
7. Xin, S.; Shen, J.; Liu, G.; Chen, Q.; Xiao, Z.; Zhang, G.; Xin, Y. Electricity Generation and Microbial Community of Single-Chamber Microbial Fuel Cells in Response to Cu_2O Nanoparticles/Reduced Graphene Oxide as Cathode Catalyst. *Chem. Eng. J.* **2020**, *380*, 122446. [CrossRef]
8. Fukuta, M.; Ono, A.; Nawa, Y.; Inami, W.; Shen, L.; Kawata, Y.; Terekawa, S. Cell Structure Imaging with Bright and Homogeneous Nanometric Light Source. *J. Biophotonics* **2017**, *10*, 503–510. [CrossRef]
9. Galanzha, E.I.; Nedosekin, D.A.; Sarimollaoglu, M.; Orza, A.I.; Biris, A.S.; Verkhusha, V.V.; Zharov, V.P. Photoacoustic and Photothermal Cytometry Using Photoswitchable Proteins and Nanoparticles with Ultrasharp Resonances. *J. Biophotonics* **2015**, *8*, 81–93. [CrossRef]
10. Kim, S.J.; Jang, D.-J. Laser-Induced Nanowelding of Gold Nanoparticles. *Appl. Phys. Lett.* **2005**, *86*, 33112. [CrossRef]
11. Zhao, Z.-J.; Shin, S.-H.; Choi, D.-G.; Park, S.-H.; Jeong, J.-H. Shape-Controlled 3D Periodic Metal Nanostructures Fabricated via Nanowelding. *Small* **2018**, *14*, 1703102. [CrossRef]
12. Rogers, A.; Niyonshuti, I.I.; Cai, A.; Wang, F.; Benamara, M.; Chen, J.; Wang, Y. Real-Time Imaging of Laser-Induced Nanowelding of Silver Nanoparticles in Solution. *J. Phys. Chem. C* **2021**, *125*, 10422–10430. [CrossRef]
13. Hu, A.; Zhou, Y.; Duley, W. Femtosecond Laser-Induced Nanowelding: Fundamentals and Applications. *Open Surf. Sci. J.* **2011**, *3*, 42–49. [CrossRef]
14. Li, M.; Xie, X.; Xu, Y.; Liu, J.; Fu, Y.; Han, M.; Li, X.; Duan, X.; Min, C.; Hu, J. External Field-Strengthened Ostwald Nanowelding. *Nano Res.* **2022**, *15*, 4525–4535. [CrossRef]
15. Garnett, E.C.; Cai, W.; Cha, J.J.; Mahmood, F.; Connor, S.T.; Greyson Christoforo, M.; Cui, Y.; McGehee, M.D.; Brongersma, M.L. Self-Limited Plasmonic Welding of Silver Nanowire Junctions. *Nat. Mater.* **2012**, *11*, 241–249. [CrossRef] [PubMed]
16. González-Rubio, G.; Guerrero-Martínez, A.; Liz-Marzán, L.M. Reshaping, Fragmentation, and Assembly of Gold Nanoparticles Assisted by Pulse Lasers. *Acc. Chem. Res.* **2016**, *49*, 678–686. [CrossRef] [PubMed]
17. Cha, S.-H.; Park, Y.; Han, J.W.; Kim, K.; Kim, H.-S.; Jang, H.-L.; Cho, S. Cold Welding of Gold Nanoparticles on Mica Substrate: Self-Adjustment and Enhanced Diffusion. *Sci. Rep.* **2016**, *6*, 32951. [CrossRef]
18. Cha, S.-H.; Kang, S.-H.; Lee, Y.J.; Kim, J.-H.; Ahn, E.-Y.; Park, Y.; Cho, S. Fabrication of Nanoribbons by Dielectrophoresis Assisted Cold Welding of Gold Nanoparticles on Mica Substrate. *Sci. Rep.* **2019**, *9*, 3629. [CrossRef]
19. Cui, J.; Theogene, B.; Wang, X.; Mei, X.; Wang, W.; Wang, K. Molecular Dynamics Study of Nanojoining between Axially Positioned Ag Nanowires. *Appl. Surf. Sci.* **2016**, *378*, 57–62. [CrossRef]
20. Lagrange, M.; Langley, D.P.; Giusti, G.; Jiménez, C.; Bréchet, Y.; Bellet, D. Optimization of Silver Nanowire-Based Transparent Electrodes: Effects of Density, Size and Thermal Annealing. *Nanoscale* **2015**, *7*, 17410–17423. [CrossRef]
21. Song, T.-B.; Chen, Y.; Chung, C.-H.; Yang, Y.M.; Bob, B.; Duan, H.-S.; Li, G.; Tu, K.-N.; Huang, Y.; Yang, Y. Nanoscale Joule Heating and Electromigration Enhanced Ripening of Silver Nanowire Contacts. *ACS Nano* **2014**, *8*, 2804–2811. [CrossRef]
22. Tseng, J.-Y.; Lee, L.; Huang, Y.-C.; Chang, J.-H.; Su, T.-Y.; Shih, Y.-C.; Lin, H.-W.; Chueh, Y.-L. Pressure Welding of Silver Nanowires Networks at Room Temperature as Transparent Electrodes for Efficient Organic Light-Emitting Diodes. *Small* **2018**, *14*, 1800541. [CrossRef] [PubMed]
23. Kim, J.; Nam, Y.S.; Song, M.H.; Park, H.W. Large Pulsed Electron Beam Welded Percolation Networks of Silver Nanowires for Transparent and Flexible Electrodes. *ACS Appl. Mater. Interfaces* **2016**, *8*, 20938–20945. [CrossRef] [PubMed]
24. Jin, R.; Cao, Y.; Mirkin, C.A.; Kelly, K.L.; Schatz, G.C.; Zheng, J.G. Photoinduced Conversion of Silver Nanospheres to Nanoprisms. *Science* **2001**, *294*, 1901–1903. [CrossRef] [PubMed]
25. Jin, R.; Charles Cao, Y.; Hao, E.; Métraux, G.S.; Schatz, G.C.; Mirkin, C.A. Controlling Anisotropic Nanoparticle Growth through Plasmon Excitation. *Nature* **2003**, *425*, 487–490. [CrossRef] [PubMed]
26. Catone, D.; Ciavardini, A.; Di Mario, L.; Paladini, A.; Toschi, F.; Cartoni, A.; Fratoddi, I.; Venditti, I.; Alabastri, A.; Proietti Zaccaria, R.; et al. Plasmon Controlled Shaping of Metal Nanoparticle Aggregates by Femtosecond Laser-Induced Melting. *J. Phys. Chem. Lett.* **2018**, *9*, 5002–5008. [CrossRef] [PubMed]

27. Herrmann, L.O.; Valev, V.K.; Tserkezis, C.; Barnard, J.S.; Kasera, S.; Scherman, O.A.; Aizpurua, J.; Baumberg, J.J. Threading Plasmonic Nanoparticle Strings with Light. *Nat. Commun.* **2014**, *5*, 4568. [CrossRef]
28. Zhang, D.; Gökce, B.; Barcikowski, S. Laser Synthesis and Processing of Colloids: Fundamentals and Applications. *Chem. Rev.* **2017**, *117*, 3990–4103. [CrossRef]
29. Rycenga, M.; Cobley, C.M.; Zeng, J.; Li, W.; Moran, C.H.; Zhang, Q.; Qin, D.; Xia, Y. Controlling the Synthesis and Assembly of Silver Nanostructures for Plasmonic Applications. *Chem. Rev.* **2011**, *111*, 3669–3712. [CrossRef]
30. Chao, C.-T.C.; Kooh, M.R.R.; Lim, C.M.; Thotagamuge, R.; Mahadi, A.H.; Chau, Y.-F.C. Visible-Range Multiple-Channel Metal-Shell Rod-Shaped Narrowband Plasmonic Metamaterial Absorber for Refractive Index and Temperature Sensing. *Micromachines* **2023**, *14*, 340. [CrossRef]
31. Chao, C.-T.C.; Kooh, M.R.R.; Chau, Y.-F.C.; Thotagamuge, R. Susceptible Plasmonic Photonic Crystal Fiber Sensor with Elliptical Air Holes and External-Flat Gold-Coated Surface. *Photonics* **2022**, *9*, 916. [CrossRef]
32. Ru, E.C.L.; Etchegoin, P.G. *Principles of Surface-Enhanced Raman Spectroscopy: And Related Plasmonic Effects*; Elsevier Science & Technology Books: Amsterdam, The Netherlands, 2009; ISBN 978-0-444-52779-0.
33. Kuppe, C.; Rusimova, K.R.; Ohnoutek, L.; Slavov, D.; Valev, V.K. "Hot" in Plasmonics: Temperature-Related Concepts and Applications of Metal Nanostructures. *Adv. Opt. Mater.* **2020**, *8*, 1901166. [CrossRef]
34. Ghosh, S.K.; Pal, T. Interparticle Coupling Effect on the Surface Plasmon Resonance of Gold Nanoparticles: From Theory to Applications. *Chem. Rev.* **2007**, *107*, 4797–4862. [CrossRef] [PubMed]
35. Marchuk, K.; Willets, K.A. Localized Surface Plasmons and Hot Electrons. *Chem. Phys.* **2014**, *445*, 95–104. [CrossRef]
36. Petryayeva, E.; Krull, U.J. Localized Surface Plasmon Resonance: Nanostructures, Bioassays and Biosensing—A Review. *Anal. Chim. Acta* **2011**, *706*, 8–24. [CrossRef]
37. Zhang, Q.; Li, W.; Moran, C.; Zeng, J.; Chen, J.; Wen, L.-P.; Xia, Y. Seed-Mediated Synthesis of Ag Nanocubes with Controllable Edge Lengths in the Range of 30-200 Nm and Comparison of Their Optical Properties. *J. Am. Chem. Soc.* **2010**, *132*, 11372–11378. [CrossRef]
38. Haque, M.A.; Imamura, R.; Brown, G.A.; Krishnamurthi, V.R.; Niyonshuti, I.I.; Marcelle, T.; Mathurin, L.E.; Chen, J.; Wang, Y. An Experiment-Based Model Quantifying Antimicrobial Activity of Silver Nanoparticles onEscherichia Coli. *RSC Adv.* **2017**, *7*, 56173–56182. [CrossRef]
39. Alqahtany, M.; Khadka, P.; Niyonshuti, I.; Krishnamurthi, V.R.; Sadoon, A.A.; Challapalli, S.D.; Chen, J.; Wang, Y. Nanoscale Reorganizations of Histone-like Nucleoid Structuring Proteins in Escherichia Coli Are Caused by Silver Nanoparticles. *Nanotechnology* **2019**, *30*, 385101. [CrossRef]
40. Niyonshuti, I.I.; Krishnamurthi, V.R.; Okyere, D.; Song, L.; Benamara, M.; Tong, X.; Wang, Y.; Chen, J. Polydopamine Surface Coating Synergizes the Antimicrobial Activity of Silver Nanoparticles. *ACS Appl. Mater. Interfaces* **2020**, *12*, 40067–40077. [CrossRef]
41. Laramy, C.R.; Brown, K.A.; O'Brien, M.N.; Mirkin, C.A. High-Throughput, Algorithmic Determination of Nanoparticle Structure from Electron Microscopy Images. *ACS Nano* **2015**, *9*, 12488–12495. [CrossRef]
42. Selvin, P.R.; Ha, T. *Single Molecule Techniques: A Laboratory Manual*, 1st ed.; Cold Spring Harbor Laboratory Press: Cold Spring Harbor, NY, USA, 2007; ISBN 0-87969-775-X.
43. Wang, Y.; Cai, E.; Sheung, J.; Lee, S.H.; Teng, K.W.; Selvin, P.R. Fluorescence Imaging with One-Nanometer Accuracy (FIONA). *J. Vis. Exp.* **2014**, *91*, 51774. [CrossRef]
44. Ashenfelter, B.A.; Desireddy, A.; Yau, S.H.; Goodson, T.; Bigioni, T.P. Fluorescence from Molecular Silver Nanoparticles. *J. Phys. Chem. C* **2015**, *119*, 20728–20734. [CrossRef]
45. Yeshchenko, O.A.; Dmitruk, I.M.; Alexeenko, A.A.; Losytskyy, M.Y.; Kotko, A.V.; Pinchuk, A.O. Size-Dependent Surface-Plasmon-Enhanced Photoluminescence from Silver Nanoparticles Embedded in Silica. *Phys. Rev. B* **2009**, *79*, 235438. [CrossRef]
46. Edelstein, A.; Amodaj, N.; Hoover, K.; Vale, R.; Stuurman, N. Computer Control of Microscopes Using μManager. *Curr Protoc Mol Biol* **2010**, *92*, 14.20.1–14.20.17. [CrossRef]
47. Edelstein, A.D.; Tsuchida, M.A.; Amodaj, N.; Pinkard, H.; Vale, R.D.; Stuurman, N. Advanced Methods of Microscope Control Using μManager Software. *J. Biol. Methods* **2014**, *1*, e10. [CrossRef] [PubMed]
48. van der Walt, S.; Schönberger, J.L.; Nunez-Iglesias, J.; Boulogne, F.; Warner, J.D.; Yager, N.; Gouillart, E.; Yu, T. Scikit-image contributors Scikit-Image: Image Processing in Python. *PeerJ* **2014**, *2*, e453. [CrossRef] [PubMed]
49. Sternberg. Biomedical Image Processing. *Computer* **1983**, *16*, 22–34. [CrossRef]
50. Kanopoulos, N.; Vasanthavada, N.; Baker, R.L. Design of an Image Edge Detection Filter Using the Sobel Operator. *IEEE J. Solid-State Circuits* **1988**, *23*, 358–367. [CrossRef]
51. Nosal, E. Flood-Fill Algorithms Used for Passive Acoustic Detection and Tracking. In Proceedings of the 2008 New Trends for Environmental Monitoring Using Passive Systems, Hyeres, France, 14–17 October 2008; pp. 1–5.
52. Kindratenko, V.V. On Using Functions to Describe the Shape. *J. Math. Imaging Vis.* **2003**, *18*, 225–245. [CrossRef]
53. Braden, B. The Surveyor's Area Formula. *Coll. Math. J.* **1986**, *17*, 326–337. [CrossRef]
54. Wang, Y.; Zocchi, G. Shape of Fair Weather Clouds. *Phys. Rev. Lett.* **2010**, *104*, 118502. [CrossRef]
55. Hohenester, U.; Trügler, A. MNPBEM—A Matlab Toolbox for the Simulation of Plasmonic Nanoparticles. *Comput. Phys. Commun.* **2012**, *183*, 370–381. [CrossRef]

56. Waxenegger, J.; Trügler, A.; Hohenester, U. Plasmonics Simulations with the MNPBEM Toolbox: Consideration of Substrates and Layer Structures. *Comput. Phys. Commun.* **2015**, *193*, 138–150. [CrossRef]
57. Hohenester, U. Simulating Electron Energy Loss Spectroscopy with the MNPBEM Toolbox. *Comput. Phys. Commun.* **2014**, *185*, 1177–1187. [CrossRef]
58. Haiss, W.; Thanh, N.T.K.; Aveyard, J.; Fernig, D.G. Determination of Size and Concentration of Gold Nanoparticles from UV−Vis Spectra. *Anal. Chem.* **2007**, *79*, 4215–4221. [CrossRef] [PubMed]
59. Paramelle, D.; Sadovoy, A.; Gorelik, S.; Free, P.; Hobley, J.; Fernig, D.G. A Rapid Method to Estimate the Concentration of Citrate Capped Silver Nanoparticles from UV-Visible Light Spectra. *Analyst* **2014**, *139*, 4855–4861. [CrossRef] [PubMed]
60. Sørensen, L.K.; Khrennikov, D.E.; Gerasimov, V.S.; Ershov, A.E.; Polyutov, S.P.; Karpov, S.V.; Ågren, H. Nature of the Anomalous Size Dependence of Resonance Red Shifts in Ultrafine Plasmonic Nanoparticles. *J. Phys. Chem. C* **2022**, *126*, 16804–16814. [CrossRef]
61. Draine, B.T.; Flatau, P.J. Discrete-Dipole Approximation for Periodic Targets: Theory and Tests. *J. Opt. Soc. Am. A* **2008**, *25*, 2693–2703. [CrossRef]
62. Draine, B.T.; Flatau, P.J. User Guide for the Discrete Dipole Approximation Code DDSCAT 7.3. *arXiv* **2013**, arXiv:1305.6497.
63. Agrawal, A.; Cho, S.H.; Zandi, O.; Ghosh, S.; Johns, R.W.; Milliron, D.J. Localized Surface Plasmon Resonance in Semiconductor Nanocrystals. *Chem. Rev.* **2018**, *118*, 3121–3207. [CrossRef]
64. Chao, C.-T.C.; Chau, Y.-F.C.; Chiang, H.-P. Highly Sensitive Metal-Insulator-Metal Plasmonic Refractive Index Sensor with a Centrally Coupled Nanoring Containing Defects. *J. Phys. D Appl. Phys.* **2021**, *54*, 115301. [CrossRef]
65. Amicucci, C.; D'Andrea, C.; de Angelis, M.; Banchelli, M.; Pini, R.; Matteini, P. Cost Effective Silver Nanowire-Decorated Graphene Paper for Drop-On SERS Biodetection. *Nanomaterials* **2021**, *11*, 1495. [CrossRef] [PubMed]
66. Kim, S.; Jin, J.; Kim, Y.-J.; Park, I.-Y.; Kim, Y.; Kim, S.-W. High-Harmonic Generation by Resonant Plasmon Field Enhancement. *Nature* **2008**, *453*, 757–760. [CrossRef] [PubMed]
67. Zhang, A.; Zhang, J.; Fang, Y. Photoluminescence from Colloidal Silver Nanoparticles. *J. Lumin.* **2008**, *128*, 1635–1640. [CrossRef]
68. He, H.; Xie, C.; Ren, J. Nonbleaching Fluorescence of Gold Nanoparticles and Its Applications in Cancer Cell Imaging. *Anal. Chem.* **2008**, *80*, 5951–5957. [CrossRef] [PubMed]
69. Geddes, C.D.; Parfenov, A.; Gryczynski, I.; Lakowicz, J.R. Luminescent Blinking of Gold Nanoparticles. *Chem. Phys. Lett.* **2003**, *380*, 269–272. [CrossRef]
70. Geddes, C.D.; Parfenov, A.; Lakowicz, J.R. Luminescent Blinking from Noble-Metal Nanostructures: New Probes for Localization and Imaging. *J. Fluoresc.* **2003**, *13*, 297–299. [CrossRef]
71. Gaiduk, A.; Ruijgrok, P.V.; Yorulmaz, M.; Orrit, M. Making Gold Nanoparticles Fluorescent for Simultaneous Absorption and Fluorescence Detection on the Single Particle Level. *Phys. Chem. Chem. Phys.* **2010**, *13*, 149–153. [CrossRef]
72. Wolfbeis, O.S. An Overview of Nanoparticles Commonly Used in Fluorescent Bioimaging. *Chem. Soc. Rev.* **2015**, *44*, 4743–4768. [CrossRef]
73. Qing, Z.; He, X.; Qing, T.; Wang, K.; Shi, H.; He, D.; Zou, Z.; Yan, L.; Xu, F.; Ye, X.; et al. Poly(Thymine)-Templated Fluorescent Copper Nanoparticles for Ultrasensitive Label-Free Nuclease Assay and Its Inhibitors Screening. *Anal. Chem.* **2013**, *85*, 12138–12143. [CrossRef]
74. Verbruggen, S.W.; Keulemans, M.; Martens, J.A.; Lenaerts, S. Predicting the Surface Plasmon Resonance Wavelength of Gold–Silver Alloy Nanoparticles. *J. Phys. Chem. C* **2013**, *117*, 19142–19145. [CrossRef]
75. Kelly, K.L.; Coronado, E.; Zhao, L.L.; Schatz, G.C. The Optical Properties of Metal Nanoparticles: The Influence of Size, Shape, and Dielectric Environment. *J. Phys. Chem. B* **2003**, *107*, 668–677. [CrossRef]
76. Ha, J.; Lee, B.J.; Hwang, D.J.; Kim, D. Femtosecond Laser Nanowelding of Silver Nanowires for Transparent Conductive Electrodes. *RSC Adv.* **2016**, *6*, 86232–86239. [CrossRef]
77. Xu, F.; Xu, W.; Mao, B.; Shen, W.; Yu, Y.; Tan, R.; Song, W. Preparation and Cold Welding of Silver Nanowire Based Transparent Electrodes with Optical Transmittances > 90% and Sheet Resistances < 10 Ohm/Sq. *J. Colloid Interface Sci.* **2018**, *512*, 208–218. [CrossRef] [PubMed]
78. Shou, W.; Mahajan, B.K.; Ludwig, B.; Yu, X.; Staggs, J.; Huang, X.; Pan, H. Low-Cost Manufacturing of Bioresorbable Conductors by Evaporation–Condensation-Mediated Laser Printing and Sintering of Zn Nanoparticles. *Adv. Mater.* **2017**, *29*, 1700172. [CrossRef]
79. Shou, W.; Pan, H. Direct Printing of Microstructures by Femtosecond Laser Excitation of Nanocrystals in Solution. *Appl. Phys. Lett.* **2016**, *108*, 214101. [CrossRef]
80. Podder, C.; Gong, X.; Yu, X.; Shou, W.; Pan, H. Submicron Metal 3D Printing by Ultrafast Laser Heating and Induced Ligand Transformation of Nanocrystals. *ACS Appl. Mater. Interfaces* **2021**, *13*, 42154–42163. [CrossRef]